optica

High-order nonlinear dipole response characterized by extreme ultraviolet ellipsometry

Kuang-Yu Chang,[1] Long-Cheng Huang,[1] Koji Asaga,[2,3] Ming-Shian Tsai,[1] Laura Rego,[4] Pei-Chi Huang,[1] Hiroki Mashiko,[2] Katsuya Oguri,[2] Carlos Hernández-García,[4] and Ming-Chang Chen[1,5,6,*]

[1]Institute of Photonics Technologies, National Tsing Hua University, Hsinchu, Taiwan
[2]NTT Basic Research Laboratories, 3-1 Morinosato Wakamiya, Atsugi, Kanagawa 243-0198, Japan
[3]Department of Electronic Engineering, Tokyo Denki University, 5 Senju-Asahi-cho, Adachi-ku, Tokyo 120-8551, Japan
[4]Grupo de Investigación en Aplicaciones del Láser y Fotónica, Departamento de Física Aplicada, University of Salamanca, Salamanca, Spain
[5]Department of Physics, National Tsing Hua University, Hsinchu, Taiwan
[6]Frontier Research Center on Fundamental and Applied Sciences of Matters, National Tsing Hua University, Hsinchu, Taiwan
*Corresponding author: mingchang@mx.nthu.edu.tw

Received 28 October 2020; revised 3 February 2021; accepted 5 February 2021 (Doc. ID 413531); published 6 April 2021

Polarization engineering and characterization of coherent high-frequency radiation are essential to investigate and control the symmetry properties of light–matter interaction phenomena at their most fundamental scales. This work demonstrates that polarization control and characterization of high-harmonic generation provides an excellent ellipsometry tool that can fully retrieve both the amplitude and phase of a strong-field-driven dipole response. The polarization control of high-harmonic generation is realized by a transient nonlinear dipole grating coherently induced by two noncollinear counterrotating laser fields. By adjusting the ellipticity of the two driving pulses simultaneously, the polarization state of every high-harmonic order can be tuned from linear to highly elliptical, and it is fully characterized through an energy-resolved extreme ultraviolet polarimeter. From the analysis of the polarization state, the ellipsometry indicated that both the amplitude and phase of the high-harmonic dipole scale rapidly with the driving laser field for higher-order harmonics, and, especially, for gases with a small ionization potential. Our experimental results were corroborated by theoretical simulations. Our findings revealed a novel high-harmonic ellipsometry technique that can be used for the next generation of high-harmonic spectroscopy and attosecond metrology studies because of its ability to provide single-digit attosecond accuracy. Our work also paves the way to precisely quantify the strong-field dynamics of fundamental processes associated with the transfer of energy and angular momentum between electron/spin systems and the symmetry-dependent properties of molecules and materials.

https://doi.org/10.1364/OPTICA.413531

1. INTRODUCTION

High-order harmonic generation (HHG), first observed in 1987 [1], describes a frequency upconversion technique in which an intense driving laser is focused into an atomic, molecular, or solid target. As a result of the laser–matter interaction, harmonic frequencies of the driving laser are emitted at the attosecond time scale. HHG in atomic gases can be intuitively understood as a sequence of three steps [2,3]: (i) tunnel ionization of the target, creating an electronic wave packet in the continuum; (ii) acceleration of the electronic wave packet by the strong laser field; and (iii) recombination of the electronic wave packet with the parent ion, with the emission of an attosecond burst of extreme ultraviolet (EUV) coherent light. At the core of the HHG process is the coherent nature of the electronic wave-packet dynamics driven by the intense laser field [4], able to produce a highly coherent beam of high-frequency harmonics of the fundamental field. HHG thus provides a tabletop ultrashort source of EUV/x-ray radiation emitted at the attosecond time scale, which has enabled a wide range of applications, such as for studying ultrafast molecular dissociation [5], for characterizing nanoscale heat flow [6], for following element-specific dynamics in magnetic materials [7,8], and for high-resolution coherent imaging [9,10]. Moreover, HHG can also be driven in molecular or solid targets, in which the emitted EUV radiation encodes unique information about the electronic and geometric arrangements of the radiating molecules or solid systems. This gives rise to self-probing schemes that allow the performance of molecular tomography [11,12], chirality assignment [13–15], and retrieval of the electronic band structure in solids [16].

Remarkably, the quantum wave-packet dynamics leave a unique signature in the phase of the emitted HHG radiation, the so-called dipole phase [17], which influences the wavefront

[18,19], spectrum [20], and pulse duration of the emitted attosecond radiation [21]. Intriguingly, the dipole phase is sensitive to the laser field, enabling applications of direct E-field reconstruction [22,23] and light-assisted phase-matching of HHG [24,25]. As a consequence, precise measurements can extract quantitative information about the absolute dipole response—both amplitude and phase—that is essential to explain the quantum dynamics of the HHG process and to advance attosecond science.

Currently, the characterization of the high-harmonic dipole response has followed two main approaches: spectroscopy and interferometry. Spectroscopic methods are based on the spectral modulation of HHG as a function of the driving laser intensity, attributed to the interference between short- and long-quantum paths [26–28]. However, a strong quantum path dependence of the spectrum and wavefront might affect the fringe visibility [29,30]. Thus, the spectral phase information is not fully retrieved from the measured HHG spectra. Interferometric techniques make use of two separate HHG sources interfering with each other, but this approach is also challenging because undesirable mechanical vibrations strongly influence the stability of the fringes [31]. Furthermore, one must devote extreme attention to avoid nonlinear effects in the transmission elements (e.g., the beam splitter, polarizer, wave plate, and vacuum window) when designing the interferometer because any laser-induced change of the refraction index can unbalance two interferometric arms, resulting in a fringe shift [32]. For instance, when two driving fields pass through the same fused-silica window (of thickness 1 mm), a 1 μJ energy difference between them is enough to induce an effective path difference of 2 nm (corresponding to a temporal shift of ≈6.6 as in time) because of the self-phase-modulation effect (assuming a beam size of diameter 1 mm and a pulse duration of 30 fs). Additionally, in HHG experiments, one must account for the macroscopic phase-matching picture, in which the radiation emitted from many—trillions of—single emitters at the target are coherently combined. The differences in the properties of emission radiated at each single atom, which depend strongly on the driving beam mode, might hinder the investigation of the quantum wave-packet dynamics. Thus, extracting accurate information about the dipole response taking place in each emitter remains challenging.

Very recently, we found that the high-order harmonic (HH) dipole phase is a key element that enables the polarization control of attosecond pulses in noncollinear HHG geometry [33]. These results, which provide a unique control rule over the ellipticity of EUV radiation, also establish a strong link between the HH dipole phase and HH polarization, motivating the use of ellipsometry as a novel technique to characterize the HH dipole response. In the late 19th century, Drude first used the phase shift induced between mutually perpendicular components of polarized light to measure the film thickness, which could be considered the birth of ellipsometry. Currently, ellipsometry is one of the most precise and accurate measurement tools and has been widely used in diverse applications such as thin-film characterization, surface molecular imaging, ion-sensing engineering, and integrated circuit technology [34,35]. However, its application in the EUV regime is challenging because of absorption limitations.

In this work, we introduce HH ellipsometry to unveil the complicated dipole dynamics of HHG through the polarization properties of EUV harmonics. Our findings reveal that the single-atom response in HHG, dominated by the short-quantum path, is the primary mechanism behind polarization control when the driving field is arranged in a noncollinear geometry. This allows us to circumvent the macroscopic picture and to use HH ellipsometry to quantify both the amplitude and phase of the HH dipole, tailored by the fundamental driving field. By adding a diffraction element into our EUV polarimeter [see Fig. 1(a) and Supplement 1, Section 1], we can fully resolve the polarization state (the helicity, ellipticity, tilt angle, and degree of polarization) for every high-harmonic order simultaneously. To the best of our knowledge, this is the first all-optical energy-resolved EUV polarimeter in the EUV field, differing from previously published EUV polarimeter and polarizer work—in which only monochromatic light was measured [33,35,36] or only an upper bound of the ellipticity was provided without knowing the helicity [37,38], and molecular polarimetry [39,40]—which requires a detailed knowledge of the light–molecule interaction.

We show that the polarization control scaling rule found in [33] ($\varepsilon_{\mathrm{EUV}} \propto \varepsilon_{\mathrm{IR}}^{\sigma}$, where $\varepsilon_{\mathrm{EUV}}$ and $\varepsilon_{\mathrm{IR}}$ are the ellipticity of the EUV high-harmonics and infrared (IR) driving field, respectively, and σ is the ellipticity scaling coefficient) depends on not only the harmonic order but also the gaseous species. The ellipticity scaling coefficient σ becomes much larger for higher-order harmonics, especially in atoms of a large atomic number (Z) with a small ionization potential. Ellipsometry retrieval quantitatively shows that the polarization control scaling depends on the effective order of nonlinearity of the high-order harmonics (q_{eff}) and on the intensity-dependent dipole phase coefficient (α), which varies substantially with harmonic order and atomic elements. Remarkably, this study also shows that the power scaling of HHG is highly influenced by the dipole phase. The variation of the dipole phase induced by any inhomogeneity in the driving laser considerably limits the attainable EUV flux and harmonic order. The homogeneity of the driving field becomes essential to achieve high HHG brightness and to extend harmonic energies toward higher frequencies.

2. EXPERIMENTAL RESULTS OF HIGH-HARMONIC ELLIPSOMETRY

We performed HHG in Ar, Kr, and Xe using 35 fs Ti:Sapphire laser pulses arranged in a noncollinear geometry (see Methods and Supplement 1, Section 2). To control the polarization of the HH pulses, two elliptically polarized fundamental beams of the same ellipticity, but opposite helicity, were noncollinearly focused into a gas jet, as shown in Fig. 1(a).

We optimized the HHG in the same spectral range in Ar, Kr, and Xe to directly compare their HH dipole response; Supplement 1 Fig. S3 shows their harmonic spectra. Figure 2 and Supplement 1 Fig. S4 show the HH ellipsometry experimental measurements, including the helicity, ellipticity ($\varepsilon_{\mathrm{EUV}}$), tilt angle ($\tau$), and degree of polarization of the EUV harmonics driven by fundamental fields with varied ellipticities ($\varepsilon_{\mathrm{IR}}$). Our results showed the two counter-rotating HH beams to be mirror symmetrically tilted with respect to the major axis of the fundamental beams (y direction), in agreement with the rotational symmetry property of noble gas atoms. Both τ and $\varepsilon_{\mathrm{EUV}}$ of each harmonic order were scaled disparately, depending on the gaseous species. The complete harmonic-order-dependent ellipticity scaling could be approximated as power relations, as shown in Table 1. When $\varepsilon_{\mathrm{IR}}$ decreased, $\varepsilon_{\mathrm{EUV}}$ decreased more rapidly for higher-order harmonics, especially in high-Z atoms. Higher-order harmonics exhibited a larger tilt-angle τ in

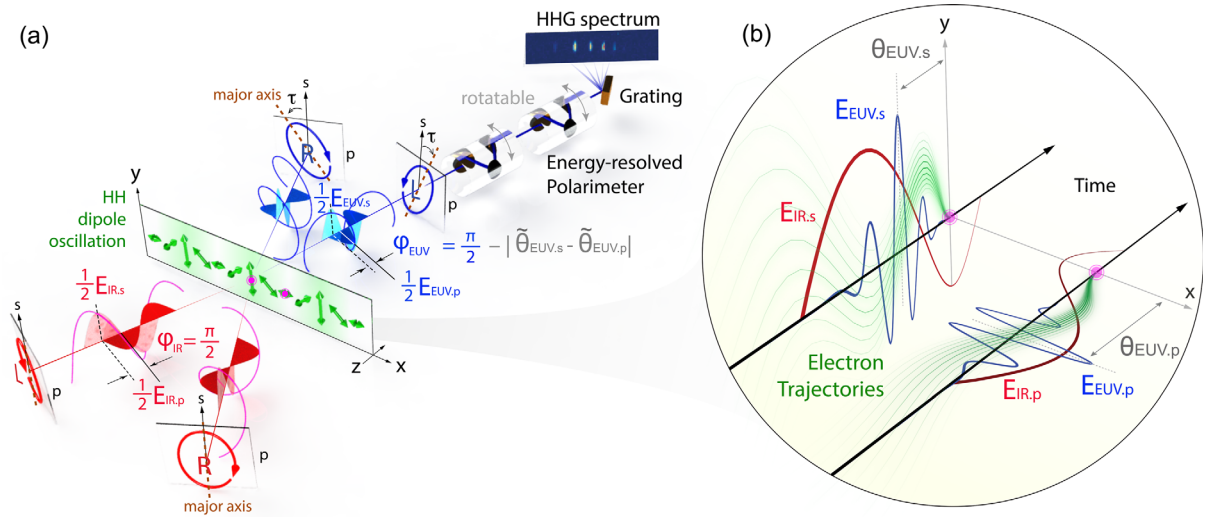

Fig. 1. HH ellipsometry technique is based on interferometry between $E_{\mathrm{EUV}\cdot p}$ and $E_{\mathrm{EUV}\cdot s}$. One can obtain the ratio of intensities and phase shift between $E_{\mathrm{EUV}\cdot p}$ and $E_{\mathrm{EUV}\cdot s}$ from the tilt-angle τ and ellipticity $\varepsilon_{\mathrm{EUV}}$ of the resultant HHG polarization. (a) Two elliptically polarized fundamental beams of the same ellipticity ($E_{\mathrm{IR}\cdot p}/E_{\mathrm{IR}\cdot s} = \varepsilon_{\mathrm{IR}}$) but opposite helicity are focused into a gas jet noncollinearly. The major axis (brown dashed line) points toward the y (or s) direction. In the focal plane, two fundamentals interferingly form local E-field vectors, rotating across direction x. Each location with linearly oscillating polarization acts as a HH local dipole oscillation (green vectors), which, when superposed, constitute a pair of elliptically polarized EUV beams in the far field. An energy-resolved polarimeter is developed to measure the ellipticity $\varepsilon_{\mathrm{EUV}}$ and tilt angle τ with respect to direction y (or s) of the harmonic emissions. (b) Microscopically, high harmonics are generated through ionization, acceleration, and recombination. Both the amplitude and phase of HHG on the focal plane are coherently scaled and spatially imprinted by the driving IR vectors. We highlight only two positions—marked in magenta—in which the dipole is driven by peaks of two perpendicular fundamentals, $E_{\mathrm{IR}\cdot p}$ and $E_{\mathrm{IR}\cdot s}$ (red lines). $E_{\mathrm{EUV}\cdot p/s}$ (blue lines) and $\theta_{\mathrm{EUV}\cdot p/s}$ present the amplitude and phase response of the dipole driven by $E_{\mathrm{IR}\cdot p/s}$; $\tilde{\theta}_{\mathrm{EUV}\cdot p/s}$ presents the phase shift in the far field from the coherent sum of all HH vectors projected to the p and s polarizations, respectively.

Table 1. Ellipticity Relation between $\varepsilon_{\mathrm{EUV}}$ and $\varepsilon_{\mathrm{IR}}$, Extracted from Fig. 2(b)

Gas	23.3 eV $\varepsilon_{15\mathrm{th}}$	26.4 eV $\varepsilon_{17\mathrm{th}}$	29.5 eV $\varepsilon_{19\mathrm{th}}$	32.6 eV $\varepsilon_{21\mathrm{st}}$
Ar	$\propto \varepsilon_{\mathrm{IR}}^{2.2}$	$\propto \varepsilon_{\mathrm{IR}}^{2.8}$	$\propto \varepsilon_{\mathrm{IR}}^{4.0}$	$\propto \varepsilon_{\mathrm{IR}}^{5.8}$
Kr	$\propto \varepsilon_{\mathrm{IR}}^{2.5}$	$\propto \varepsilon_{\mathrm{IR}}^{4.0}$	$\propto \varepsilon_{\mathrm{IR}}^{5.3}$	$\propto \varepsilon_{\mathrm{IR}}^{8.3}$
Xe	$\propto \varepsilon_{\mathrm{IR}}^{5.3}$	$\propto \varepsilon_{\mathrm{IR}}^{10.2}$	$\propto \varepsilon_{\mathrm{IR}}^{13.5}$	

Ar and Kr than in Xe, the reason being that there was a much more rapid amplitude decrease in the x direction in Xe. All these phenomena are associated with the harmonic dipole response—that is, the amplitude and phase of the high-order harmonics scale with the laser field—as explained in detail in the discussion section.

To disentangle the microscopic and macroscopic nature of the HH ellipsometry results, we performed two additional experiments. First, we measured the HH yield as a function of the backing pressure, as shown in Supplement 1, Section 4 and Fig. S6. The results clearly show that the yield of every order of HHG in Ar, Kr, and Xe exhibited a quadratic dependence on pressure, indicating that plasma effects did not influence the propagation of the driving fields. Second, we showed that the polarization state of the high-order harmonics did not depend on the backing pressure of the gas jet (Supplement 1 Fig. S7). Accordingly, we concluded that the polarization control in the noncollinear geometry was not related to the propagation of the IR effect in the generating medium; the single-atom response itself was thus responsible for shaping the polarization properties of the high-order harmonics. In the following section, we reveal the relationship between the polarization scaling of HHG and its complex dipole response.

3. RETRIEVAL OF HIGH-HARMONIC DIPOLE RESPONSE FROM ELLIPSOMETRY

Straightforwardly, ellipsometry can determine the sign of the HH phase change using the tilt direction. In Fig. 2(a), all orientations of the right-handed circularly polarized harmonics tilt counterclockwise with respect to the major axis of the fundamental beams (y direction), whereas the left-handed circularly polarized harmonics tilt clockwise. This effect can be explained in terms of the weight of the s and p components of the local E-field at the focal plane, as depicted in Fig. 1(b). If $E_{\mathrm{IR}\cdot s}$ is stronger than $E_{\mathrm{IR}\cdot p}$, the induced dipole phase advance (negative sign) of $\theta_{\mathrm{EUV}\cdot s} - \theta_{\mathrm{EUV}\cdot p}$ on the focal plane makes $\varphi_{\mathrm{EUV}} = \pi/2 - |\tilde{\theta}_{\mathrm{EUV}\cdot s} - \tilde{\theta}_{\mathrm{EUV}\cdot p}| < \pi/2$, resulting in a positive tilt angle τ in the far field, as defined and marked in Fig. 1(a).

To retrieve quantitative information of the atomic dipole response from an HH ellipsometry measurement, we applied the thin-slab model (TSM), based on strong-field assumptions about the nature of the produced harmonics, which are known to provide satisfactorily qualitative results for HHG in a thin gas-jet configuration [18,19,41–43] (also described in Supplement 1, Sections 6–7). The local q order HH emission in the x and y directions at time t can be described by

$$E_{\mathrm{EUV}\cdot x}(x, y, 0, t) \propto I_{\mathrm{IR}}(x, y, t)^{\frac{q_{\mathrm{eff}}}{2}} e^{i[q\omega_{\mathrm{IR}}t - I_{\mathrm{IR}}(x,y,t)\alpha]} \times \frac{E_{\mathrm{IR}\cdot x}(x, y, 0, t)}{\sqrt{I_{\mathrm{IR}}(x, y, t)}}\hat{x}, \quad (1)$$

$$E_{\mathrm{EUV}\cdot y}(x,y,0,t) \propto I_{\mathrm{IR}}(x,y,t)^{\frac{q_{\mathrm{eff}}}{2}} e^{i[q\omega_{\mathrm{IR}}t - I_{\mathrm{IR}}(x,y,t)\alpha]} \times \frac{E_{\mathrm{IR}\cdot y}(x,y,0,t)}{\sqrt{I_{\mathrm{IR}}(x,y,t)}}\hat{y}, \quad (2)$$

where ω_{IR} is the IR angular frequency, $E_{\mathrm{IR}\cdot x}(x,y,0,t)$ and $E_{\mathrm{IR}\cdot y}(x,y,0,t)$ represent structured IR in the focal plane toward the x and y directions, respectively, and $I_{\mathrm{IR}}(x,y,t) \propto |E_{\mathrm{IR}\cdot x}(x,y,0,t)|^2 + |E_{\mathrm{IR}\cdot y}(x,y,0,t)|^2$ represents the local intensity (details are presented in the Methods section). Equations (1) and (2) are based on the dipole response of the q-order harmonic as a function of the laser field having the form $E_{\mathrm{EUV}}(I_{\mathrm{IR}}) \propto A_q(I_{\mathrm{IR}})\exp[i\theta_q(I_{\mathrm{IR}})]$, which can be well approximated as $E_{\mathrm{EUV}}(I_{\mathrm{IR}}) \propto I_{\mathrm{IR}}^{q_{\mathrm{eff}}/2}\exp[-iI_{\mathrm{IR}}\alpha]$, where $A_q(I_{\mathrm{IR}}) \cong I_{\mathrm{IR}}^{q_{\mathrm{eff}}/2}$ is the amplitude of the q-order harmonic, q_{eff} is an effective order of nonlinearity, and $\theta_q(I_{\mathrm{IR}}) \cong -I_{\mathrm{IR}}\alpha$ is the phase of the q-order harmonic. The phase shift is approximately proportional to the local intensity and has been theoretically and experimentally validated [17,23,31]. The leading negative sign indicates that an increased driving intensity advances the HHG phase, which agrees with the tilt angle direction observed in Fig. 2. The coefficient α depends strongly on the quantum path followed by the electronic wave packet during the HHG process—that is, the type (short or long), peak intensity and frequency of the driving field, harmonic order, and gaseous species. We noted that the HHG emission was dominated by the short-quantum path contribution in this study of polarization control, as discussed in Supplement 1, Section 7.

The state of polarization of high-order harmonics in the far field was obtained through the coherent sum of Eqs. (1) and (2) for s and p polarizations at the focal plane, based on the Huygens–Fresnel principle [41,42,44,45], which results in two main diffraction EUV beams. The polarization characteristics of the helicity, ellipticity $\varepsilon_{\mathrm{EUV}}$, and tilt angle τ are determined by how the EUV vector [sum of Eqs. (1) and (2)] rotates as a function of time t. Consequently, the microscopic parameters q_{eff} and α can be directly extracted through the measured EUV ellipticity $\varepsilon_{\mathrm{EUV}}$ and tilt angle τ. Using two-dimensional range queries for the minimum deviations (see Supplement 1 Section 5, Figs. S9 and S10), the effective scaling parameters in amplitude and phase, q_{eff} and α, were obtained by fitting all observations of $\varepsilon_{\mathrm{EUV}}$ and τ from Fig. 2. The statistics of all retrieved q_{eff} and α are shown in Fig. 3. It should be emphasized that all polarization measurements of HHG were extracted to have a similar characterization response in q_{eff} and α in the same HH target, validating our TSM-based retrieval model.

4. DISCUSSION

Our polarization control scheme differs significantly from those in the literature, in which interferometry of two-color counterrotating beams [40,47] or two attosecond pulses [48,49] were applied. The resulting polarization provided by these two approaches—characterized by $\varepsilon_{\mathrm{EUV}}$ and τ—can be extremely sensitive to a delay between the two arms of the interferometer. The degree p of the HHG polarization can also deteriorate due to the instability of the interferometer. Compared to the two-color counterrotating

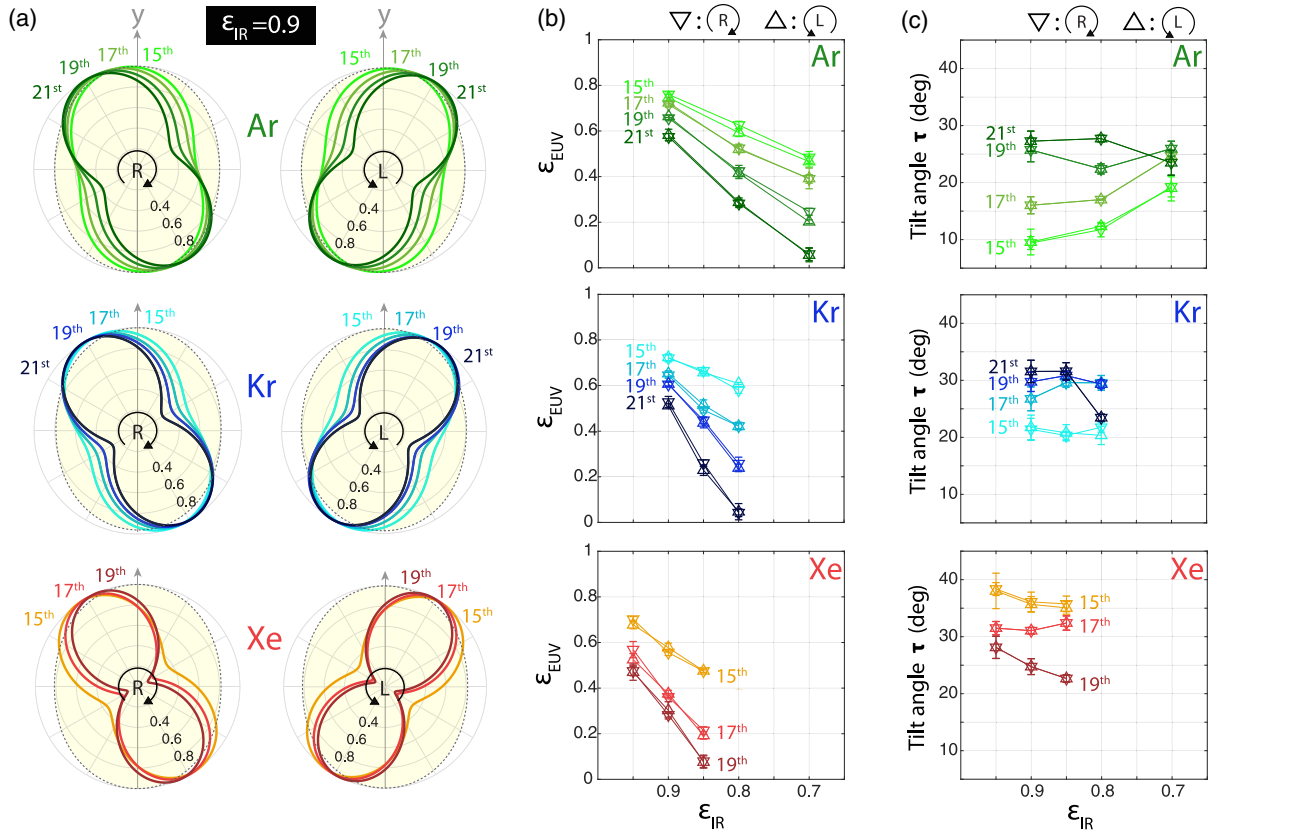

Fig. 2. Polarization scaling of HHG in Ar, Kr, and Xe. (a) The experimentally observed polarization states of HHG EUV (green lines for Ar, blue lines for Kr, and red lines for Xe) when driven by $\varepsilon_{\mathrm{IR}} = 0.9$ IR (yellow area with blask dashes) are depicted in the polar plots. Outputs (b) $\varepsilon_{\mathrm{EUV}}$ and (c) τ versus varied $\varepsilon_{\mathrm{IR}}$. The color gradient shows varied harmonic order q. The uncertainties (standard deviation) are derived from five individual measurements.

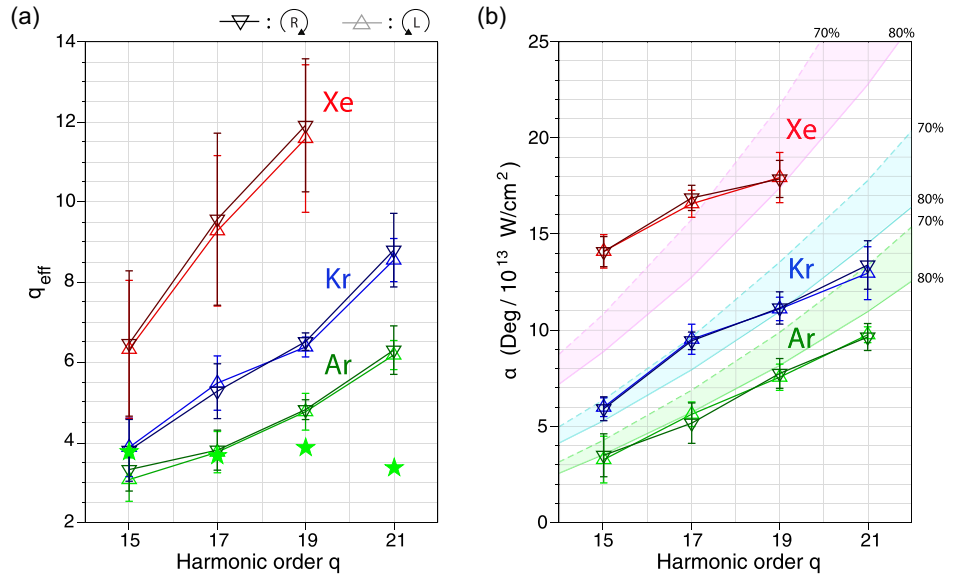

Fig. 3. Dipole response information extracted from HH ellipsometry. (a) Power scaling, q_{eff} versus harmonic order q, extracted from Ar (green), Kr (blue), and Xe (red). Green stars represent the calculated q_{eff} in Ar obtained from quantum strong-field approximation (SFA) theory, as described in [42] and Supplement 1, Section 6. This calculation uses a peak intensity, 1.2×10^{14} W/cm^2, less than the 2.8×10^{14} W/cm^2 applied in HH ellipsometry. (b) Phase-intensity slope α versus harmonic order q. Light strips mark α calculated from the semiclassical model (as indicated in [46]), using intensities 70% and 80% of their average peak intensities. The use of a reduced intensity in our simulations is attributed to nonuniformities at the experimental focus, and to remain in the tunneling regime.

scheme [40], in which p ranges from 0.4 to 0.85, and τ is unstable, we observed a high degree of polarization p in a range between 0.8 and 1 (see Supplement 1 Fig. S4). With no locking system for active stabilization of the path between two IR beams, the uncertainty of τ was only ≈1.5°, as shown in Fig. 2(c), indicating that the timing jitter between $E_{\mathrm{EUV}\cdot s}$ and $E_{\mathrm{EUV}\cdot p}$ was ≈3 as. Such excellent stability arises because our scheme is based on a transient polarization grating induced by two driving fields. Calculations show that the phase fluctuation between the two arms could easily alter the IR interference on the focal plane, but barely alter $\varepsilon_{\mathrm{EUV}}$ and τ of the EUV beams in the far field. Hence, our interferometry performs as an inline interferometer [32], in which the instability between two arms is negligible. The observed fluctuation is likely attributed to the power instability ≈1% of the driving laser as both the amplitude and phase of the HHG are coupled with the IR intensity.

Further insight was obtained by comparison with a semiclassical calculation [46,50]. The electronic dynamics in the three-step model can be approximated by integrating the classical equations of motion given by Newton's law. In the tunneling regime, one can assume that the ionization depends on only the instantaneous value of the electromagnetic field; immediately after ionization, the electron is located at the coordinate origin with zero velocity. Another assumption of this model is that the dynamics subsequent to ionization correspond to a classical free electron in the electromagnetic field, thus neglecting the influence of the Coulomb potential. Figure 4 shows the recollision kinetic energy of the electrons as a function of ionization time t_i (brown curves) and recollision time t_r (black curves). The phase of the harmonic emission depends not only on the phase of the fundamental field, but also on the particular quantum path followed by the electron. Our calculations reveal that HHG phase θ_{EUV} exhibits a piecewise-linear dependence on the electron excursion time $t_r - t_i$; the phase difference $|\theta_{\mathrm{EUV}\cdot p} - \theta_{\mathrm{EUV}\cdot s}|$ is approximately linearly proportional to the intensity difference, $\Delta I_{\mathrm{IR}} = I_{\mathrm{IR}\cdot s} - I_{\mathrm{IR}\cdot p}$, in agreement with our ellipsometry observations in Supplement 1 Fig. S11.

Figure 3 shows that α increases as a function of the harmonic order q. This is understandable because the quantum path that requires a greater kinetic energy would ionize earlier at t_i and recombine later at t_r, as shown in Fig. 4. In such a case, a greater value of the quantum phase accumulates in the process of ionization, acceleration, and recombination. Moreover, for the same

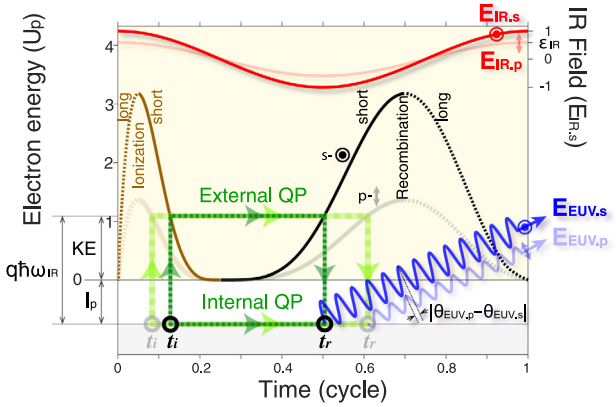

Fig. 4. Comparison of quantum paths of HHG in s and p polarizations. Output HH energy $q\hbar\omega_{\mathrm{IR}}$ is the sum of ionization potential I_p and kinetic energy (KE) gained from the driving IR field (red lines). KE just before recombination is depicted as a function of time of ionization t_i (brown curves) and recombination t_r (black curves) with a semiclassical calculation. The driving IR field is normalized to the field amplitude in s-polarization $E_{\mathrm{IR}\cdot s}$. Since $E_{\mathrm{IR}\cdot p}$ (light red line) is weak with less pondermotive energy (Up), to keep the same output energy $q\hbar\omega_{\mathrm{IR}}$—i.e., to obtain the same KE—an electron takes a longer excursion time in the continuum with an earlier t_i and a later t_r. As a result, there is a phase lag in $E_{\mathrm{EUV}\cdot p}$ (light blue line) with respect to $E_{\mathrm{EUV}\cdot s}$ (blue line) because more quantum phase is accumulated through the interference (green lines) between the external and internal quantum paths (QP).

harmonic order q, a larger α is also observed in a noble gas of large Z—the reason being that output energy $q\hbar\omega_{\mathrm{IR}}$ is the sum of ionization energy I_p overcome by the laser pulse and the kinetic energy gained from the electric force of the following field. Because I_p is smaller in a noble gas of large Z, more kinetic energy is required to maintain the same output energy $q\hbar\omega_{\mathrm{IR}}$. Electrons thus undergo a longer excursion period in the continuum, resulting in a larger HHG phase. The HHG phase dependent on I_p has also been observed in other findings in a mixed gas [51], and in 2-as pulse interference [52].

The semiclassical three-step model can also obtain α through an action integral over the electron trajectory [46], but such a calculation is based on a single-atom picture. For HHG driven with a Gaussian focus, many single emitters are excited with varied intensities. The interference effect should be considered when performing a coherent sum over all emitters. Two α curves using 70% and 80% of the average peak intensities are calculated and shown in Fig. 3(b) (their average peak intensities, $(I_{\mathrm{IR}\cdot s} + I_{\mathrm{IR}\cdot p})/2$, are listed in Supplement 1, Table S1). In Ar, α extracted from ellipsometry measurements shows quantitatively good agreement with that obtained from a semiclassical calculation, which indicates that the experimental α could be accurately estimated using 80% of the average peak intensity. Interestingly, in Kr and Xe, the slope of α obtained from ellipsometry measurements was flatter than that derived from a semiclassical calculation. Such a discrepancy between the theory and experimental results can be understood to be due to a strong variation in the beam size of HHG versus harmonic order in gases with a small ionization potential, as q_{eff} varies significantly [see Fig. 3(a)]. When HHG is driven with a Gaussian beam, higher-order harmonics with a larger q_{eff} tend to be generated nearer the center of the focus, at which the intensity is greater on average. Consequently, α should become smaller, as discussed in the preceding paragraph.

Moreover, Fig. 3(a) clearly shows that q_{eff} becomes larger in a large-Z gas. This phenomenon could be due to the tunnel ionization yield, as the single-atom yield of HHG is proportional to the ionization probability. A comparison of the ionization fraction of Ar, Kr, and Xe using the Ammosov–Delone–Krainov ionization model can be found as a function of time for a 35 fs duration pulse [53]. In a gas with a smaller ionization potential, there is a more rapid change in the fraction of ionization due to the variation of fundamental pulses—which implies that atoms with a small ionization potential have a large effective order of nonlinearity q_{eff}. Generally, a large quantum phase shift between the s and p polarization tends to enlarge the tilt angle τ, but in Xe, a much more rapid amplitude drop in p polarization leads to a small tilt-angle τ in higher-order harmonics, contrary to the τ behavior in Ar and Kr, as shown in Fig. 2. In short, q_{eff} also influences the tilt angle τ. HH ellipsometry can thus decouple and quantify the scaling of amplitude and phase with an accuracy of a few attoseconds, which differs markedly from other HH spectroscopic techniques [15,26–28,31,53]–55.

Finally, our HH ellipsometry results were validated using an alternative HHG experiment driven by a linearly polarized IR beam. Figure 5 shows a comparison of the HHG yield as a function of the driving laser intensity in Ar, Kr, and Xe. In Ar, the flux of all harmonics grew exponentially under a small IR intensity, whereas it saturated at a large intensity because of the depletion of neutral atoms, limiting the amplitude of single-atom emission. In Kr, the flux scaling of the low-order harmonics behaved similarly

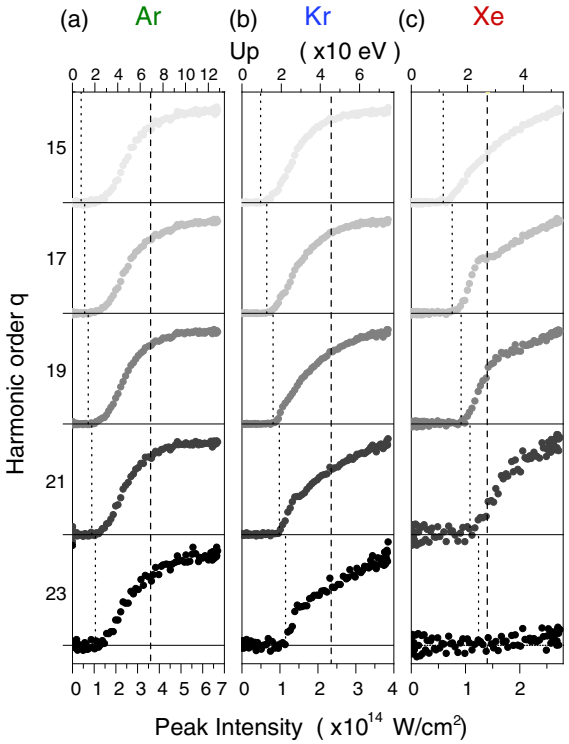

Fig. 5. Comparison of HHG yield as a function of driving laser intensity in (a) Ar, (b) Kr, and (c) Xe. The harmonic with a large phase-intensity slope α, observed in Fig. 3, also behaves more weakly and grows almost linearly with IR intensity because of the strong EUV phase variation induced by the transverse and longitudinal inhomogeneity of the IR beam. Dotted lines indicate the minimum peak intensity to generate the q-order harmonic. Dashed lines mark the peak intensity of 3.6×10^{14}, 2.35×10^{14}, and 1.4×10^{14} W/cm^2 for Ar, Kr, and Xe, respectively, that produces 50% ionization after a 35-fs IR laser field based on the Ammosov–Delone–Krainov ionization model [53].

to that in Ar, whereas the growth of the higher-order harmonics decreased gradually, becoming linearly proportional to the driving laser intensity in harmonic order 23. Such linear growth behavior occurred more significantly in Xe, for which—by comparison to the same harmonic order—the power scaling became more linear in large Z atoms in every order. It should be noted that all observed power scalings in these three gases exhibited no dependence on the backing pressure, indicating no propagation effect of IR that might have influenced the HH yield. Remarkably, these results agreed well with α, observed from the HH ellipsometry. The harmonic with a large phase-intensity slope α, as shown in Fig. 3(b), behaved much more weakly, growing almost linearly with the IR intensity. The power scaling of HHG became limited by a strong EUV phase variation induced by the intensity inhomogeneity of the driving IR in higher-order harmonics and in a gas with a small ionization potential, especially when $\alpha > 10$ deg./(10^{13} W/cm^2). It should also be emphasized that the power scaling of the single-atom response (q_{eff}) cannot be directly extracted from this yield-growth measurement, since it cannot correctly retrieve the single-atom response of HHG. Lastly, it is also interesting to note that, despite the phase of each HHG emitter varying widely in Xe, we still observed a large degree of polarization, $p \cong 0.9$, based on the polarimeter measurement, indicating that the wavefront of HHG was still stable and coherent.

5. CONCLUSIONS

We demonstrated that polarization control and characterization of HHG in a noncollinear geometry provides an excellent ellipsometry tool able to unveil the quantum dynamics of HH samples under intense laser fields. Our polarization control scheme was based on a transient polarization grating induced by two fundamental fields, being insensitive to the path fluctuation between the two arms of the driving fields and demonstrating excellent stability and single-digit attosecond accuracy. HH ellipsometry can measure two parameters—the ratio of intensities and phase difference information—compared with the single parameter of regular HH spectroscopic techniques, that is, only intensity without phase. Both the amplitude and phase of the HH dipole were precisely characterized using HH ellipsometry, carrying detailed information about the evolution of an ionized electronic wave packet. This study also clearly demonstrated how the amplitude and phase of the nonperturbative HH dipole influenced the power scaling of HHG and the achievable HH energy. Prospective future applications of HH ellipsometry should allow us to precisely quantify quantum dynamics, ultrafast chirality changes, and circular dichroism in HHG samples, as well as to enable critical comparisons with theory. This work also motivates future work to drive HH ellipsometry with structured light having tailored angular momentum and chiral properties [43,56], in which the most rapid transfer of energy and angular momentum in atoms, chiral molecules, 2D, and magnetic materials can be quantitatively resolved.

6. METHODS

A. Polarization Control of HHG in a Noncollinear Geometry

The pulse energies of the two IR arms were carefully tuned to be identical—that is, 130, 120, and 100 μJ for the Ar, Kr, and Xe gas jets, respectively. The average peak intensity of the crossing beam on the focal plane, $(I_{\mathrm{IR}\cdot s} + I_{\mathrm{IR}\cdot p})/2$, was estimated to be 2.82×10^{14}, 2.6×10^{14}, and 2.16×10^{14} W/cm^2, respectively (details of driving IR fields are shown in Supplement 1, Table S1). The tilt angle of the major axes of the driving pulses was carefully aligned toward the y direction. Each driving electric field thus consisted of two perpendicular components with an amplitude ratio and ellipticity $E_{\mathrm{IR}\cdot p}/E_{\mathrm{IR}\cdot s} = \varepsilon_{\mathrm{IR}}$, and phase shift $\varphi_{\mathrm{IR}} = \pi/2$. At the focal plane, the combination of the two noncollinear driving fields resulted in local linearly polarized E-field vectors, of which the direction rotated along the x axis. Each local linearly polarized IR field produced linearly polarized HH emission in the near field, which, upon propagation into the far field, led to a pair of elliptically polarized EUV beams. The ellipticity $\varepsilon_{\mathrm{EUV}}$ of the HH pulses—that is, the ratio of the minor axis with respect to the major axis of elliptically polarized light, and tilt angle τ of the major axis with respect to the y direction—were controlled with the fundamental ellipticity $\varepsilon_{\mathrm{IR}}$, while maintaining a good beam profile (Supplement 1, Section S3), as well as an upconversion efficiency.

B. Structured IR Light on the Focal Plane

We consider two identical elliptically polarized IR driving beams with equal ellipticity but opposite helicity [see Fig. 1(a)], given by

$$E_{\mathrm{IR}\cdot R}(x, y, z, t) = E_0 \frac{-i\varepsilon_{\mathrm{IR}}\hat{p} + \hat{s}}{\sqrt{1+\varepsilon_{\mathrm{IR}}{}^2}} \times \exp\left[-ikz\cos\xi + ikx\sin\xi + i\omega_{\mathrm{IR}}t\right], \tag{3}$$

$$E_{\mathrm{IR}\cdot L}(x, y, z, t) = E_0 \frac{i\varepsilon_{\mathrm{IR}}\hat{p} + \hat{s}}{\sqrt{1+\varepsilon_{\mathrm{IR}}{}^2}} \times \exp\left[-ikz\cos\xi - ikx\sin\xi + i\omega_{\mathrm{IR}}t\right], \tag{4}$$

where $E_{\mathrm{IR}\cdot R}$ ($E_{\mathrm{IR}\cdot L}$) represents the right-handed (left-handed) elliptically polarized IR field, E_0 is the field amplitude, $k = 2\pi/\lambda_{\mathrm{IR}}$ is the fundamental wave vector, λ_{IR} is the wavelength of the driving laser, ω_{IR} is the IR angular frequency, and ξ is the half-crossing angle between the two fundamental laser beams. As the noncollinear angle is small in the experiment ($\xi = 20.9$ mrad), $\hat{y} = \hat{s}$ and $\hat{x} = \hat{p}\cos(\xi) \cong \hat{p}$, considering a Gaussian intensity distribution (with beam waist ω_0), the electric field at the focal plane ($z = 0$) can be written as

$$\begin{aligned} E_{\mathrm{focus}}(x, y, 0, t) &\propto E_{\mathrm{IR}\cdot R}(x, y, 0, t) + E_{\mathrm{IR}\cdot L}(x, y, 0, t) \\ &= 2E_0 \frac{e^{-\left(\frac{x^2+y^2}{\omega_0^2}\right)+i\omega_{\mathrm{IR}}t}}{\sqrt{(1+\varepsilon_{\mathrm{IR}}{}^2)}} \\ &\quad \times \left[\varepsilon_{\mathrm{IR}}\sin(kx\sin\xi)\hat{x} + \cos(kx\sin\xi)\hat{y}\right] \\ &= E_{\mathrm{IR}\cdot x}(x, y, 0, t)\hat{x} + E_{\mathrm{IR}\cdot y}(x, y, 0, t)\hat{y}, \end{aligned} \tag{5}$$

in which

$$E_{\mathrm{IR}\cdot x}(x, y, 0, t) = 2E_0 \frac{\varepsilon_{\mathrm{IR}}\sin(kx\sin\xi)}{\sqrt{(1+\varepsilon_{\mathrm{IR}}^2)}} e^{-\left(\frac{x^2+y^2}{\omega_0^2}\right)+i\omega_{\mathrm{IR}}t}, \tag{6}$$

and

$$E_{\mathrm{IR}\cdot y}(x, y, 0, t) = 2E_0 \frac{\cos(kx\sin\xi)}{\sqrt{(1+\varepsilon_{\mathrm{IR}}^2)}} e^{-\left(\frac{x^2+y^2}{\omega_0^2}\right)+i\omega_{\mathrm{IR}}t}. \tag{7}$$

One calculated snapshot of the IR E-field vector distribution is shown in Supplement 1 Fig. S8. For the retrieval, the IR laser amplitude E_0, focal beam waist ω_0, half-crossing angle ξ, and ellipticity $\varepsilon_{\mathrm{IR}}$ were calibrated experimentally, and then used as an input for Eqs. (1) and (2).

Funding. Ministry of Science and Technology (109-2634-F-007-023, 109-2636-M-007-008); Ministry of Education; Japan Society for the Promotion of Science KAKENHI (JSPS) (19H02637, 20H05670); Ministerio de Ciencia e Innovación y Universidades (FIS2016-75652-P, PID2019-106910GB-I00, RYC-2017-22745); Junta de Castilla y León FEDER (SA287P18); Ministerio de Educación, Cultura y Deporte (FPU16/02591); H2020 European Research Council (ERC) (851201).

Acknowledgment. We thank Prof. Luis Plaja and Prof. C. D. Lin for fruitful discussions. The experimental work was undertaken at the National Tsing Hua University, Institute of Photonic Technologies. M.-C. C. gratefully acknowledges a Taiwan MOST Young Scholar Fellowship. K. A. acknowledges support from the Y.-S. Liu Global Talent Scholarship. H. M. and K. O. acknowledge the JSPS.

Disclosures. The authors declare no conflict of interest.

Supplemental document. See Supplement 1 for supporting content.

REFERENCES

1. A. McPherson, G. Gibson, H. Jara, U. Johann, T. S. Luk, I. A. McIntyre, K. Boyer, and C. K. Rhodes, "Studies of multiphoton production of vacuum ultraviolet-radiation in the rare-gases," J. Opt. Soc. Am. B **4**, 595–601 (1987).
2. K. J. Schafer, B. Yang, L. F. DiMauro, and K. C. Kulander, "Above threshold ionization beyond the high harmonic cutoff," Phys. Rev. Lett. **70**, 1599–1602 (1993).
3. P. B. Corkum, "Plasma perspective on strong-field multiphoton ionization," Phys. Rev. Lett. **71**, 1994–1997 (1993).
4. R. Zerne, C. Altucci, M. Bellini, M. B. Gaarde, T. W. Hänsch, A. L'Huillier, C. Lynga, and C. G. Wahlström, "Phase-locked high-order harmonic sources," Phys. Rev. Lett. **79**, 1006–1009 (1997).
5. Y. Pertot, C. Schmidt, M. Matthews, A. Chauvet, M. Huppert, V. Svoboda, A. von Conta, A. Tehlar, D. Baykusheva, J.-P. Wolf, and H. J. Wörner, "Time-resolved x-ray absorption spectroscopy with a water window high-harmonic source," Science **355**, 264–267 (2017).
6. T. D. Frazer, J. L. Knobloch, K. M. Hoogeboom-Pot, D. Nardi, W. Chao, R. W. Falcone, M. M. Murnane, H. C. Kapteyn, and J. N. Hernandez-Charpak, "Engineering nanoscale thermal transport: size- and spacing-dependent cooling of nanostructures," Phys. Rev. Appl. **11**, 024042EP (2019).
7. C. La-O-Vorakiat, M. Siemens, M. M. Murnane, H. C. Kapteyn, S. Mathias, M. Aeschlimann, P. Grychtol, R. Adam, C. M. Schneider, J. M. Shaw, H. Nembach, and T. J. Silva, "Ultrafast demagnetization dynamics at the M edges of magnetic elements observed using a tabletop high-harmonic soft x-ray source," Phys. Rev. Lett. **103**, 257402 (2009).
8. F. Siegrist, J. A. Gessner, M. Ossiander, C. Denker, Y.-P. Chang, M. C. Schröder, A. Guggenmos, Y. Cui, J. Walowski, U. Martens, J. K. Dewhurst, U. Kleinberg, M. Münzenberg, S. Sharma, and M. Schultze, "Light-wave dynamic control of magnetism," Nature **571**, 240–244 (2019).
9. O. Kfir, S. Zayko, C. Nolte, M. Sivis, M. Möller, B. Hebler, S. S. P. K. Arekapudi, D. Steil, S. Schäfer, M. Albrecht, O. Cohen, S. Mathias, and C. Ropers, "Nanoscale magnetic imaging using circularly polarized high-harmonic radiation," Sci. Adv. **3**, eaao4641 (2017).
10. D. F. Gardner, M. Tanksalvala, E. R. Shanblatt, X. Zhang, B. R. Galloway, C. L. Porter, R. Karl, Jr., C. Bevis, D. E. Adams, H. C. Kapteyn, M. M. Murnane, and G. F. Mancini, "Subwavelength coherent imaging of periodic samples using a 13.5 nm tabletop high-harmonic light source," Nat. Photonics **11**, 259–263 (2017).
11. N. L. Wagner, A. Wüest, I. P. Christov, T. Popmintchev, X. Zhou, M. M. Murnane, and H. C. Kapteyn, "Monitoring molecular dynamics using coherent electrons from high harmonic generation," Proc. Natl. Acad. Sci. USA **103**, 13279 (2006).
12. J. Itatani, J. Levesque, D. Zeidler, H. Niikura, H. Pepin, J. C. Kieffer, P. B. Corkum, and D. M. Villeneuve, "Tomographic imaging of molecular orbitals," Nature **432**, 867–871 (2004).
13. S. Beaulieu, A. Comby, A. Clergerie, J. Caillat, D. Descamps, N. Dudovich, B. Fabre, R. Géneaux, F. Légaré, S. Petit, B. Pons, G. Porat, T. Ruchon, R. Taïeb, V. Blanchet, and Y. Mairesse, "Attosecond-resolved photoionization of chiral molecules," Science **358**, 1288–1294 (2017).
14. D. Baykusheva, D. Zindel, V. Svoboda, E. Bommeli, M. Ochsner, A. Tehlar, and H. J. Wörner, "Real-time probing of chirality during a chemical reaction," Proc. Natl. Acad. Sci. USA **116**, 23923 (2019).
15. O. Neufeld, D. Ayuso, P. Decleva, M. Y. Ivanov, O. Smirnova, and O. Cohen, "Ultrasensitive chiral spectroscopy by dynamical symmetry breaking in high harmonic generation," Phys. Rev. X **9**, 031002EP (2019).
16. A. A. Lanin, E. A. Stepanov, A. B. Fedotov, and A. M. Zheltikov, "Mapping the electron band structure by intraband high-harmonic generation in solids," Optica **4**, 516–519 (2017).
17. M. Lewenstein, P. Salières, and A. L'Huillier, "Phase of the atomic polarization in high-order harmonic generation," Phys. Rev. A **52**, 4747–4754 (1995).
18. H. Wikmark, C. Guo, J. Vogelsang, P. W. Smorenburg, H. Coudert-Alteirac, J. Lahl, J. Peschel, P. Rudawski, H. Dacasa, S. Carlström, S. Maclot, M. B. Gaarde, P. Johnsson, C. L. Arnold, and A. L'Huillier, "Spatiotemporal coupling of attosecond pulses," Proc. Natl. Acad. Sci. USA **116**, 4779–4787 (2019).
19. L. Quintard, V. Strelkov, J. Vabek, O. Hort, A. Dubrouil, D. Descamps, F. Burgy, C. Péjot, E. Mével, F. Catoire, and E. Constant, "Optics-less focusing of XUV high-order harmonics," Sci. Adv. **5**, eaau7175 (2019).
20. H. J. Shin, D. G. Lee, Y. H. Cha, K.-H. Hong, and C. H. Nam, "Generation of nonadiabatic blueshift of high harmonics in an intense femtosecond laser field," Phys. Rev. Lett. **83**, 2544–2547 (1999).
21. Y. Mairesse, A. De Bohan, L. J. Frasinski, H. Merdji, L. C. Dinu, P. Monchicourt, P. Breger, M. Kovacev, R. Taïeb, B. Carré, H. G. Muller, P. Agostini, and P. Salieres, "Attosecond synchronization of high-harmonic soft x-rays," Science **302**, 1540–1543 (2003).
22. K. T. Kim, C. Zhang, A. D. Shiner, B. E. Schmidt, F. Légaré, D. M. Villeneuve, and P. B. Corkum, "Petahertz optical oscilloscope," Nat. Photonics **7**, 958–962 (2013).
23. P. Carpeggiani, M. Reduzzi, A. Comby, H. Ahmadi, S. Kühn, F. Calegari, M. Nisoli, F. Frassetto, L. Poletto, D. Hoff, J. Ullrich, C. D. Schroter, R. Moshammer, G. G. Paulus, and G. Sansone, "Vectorial optical field reconstruction by attosecond spatial interferometry," Nat. Photonics **11**, 383–389 (2017).
24. H.-W. Sun, P.-C. Huang, Y.-H. Tzeng, J.-T. Huang, C. D. Lin, C. Jin, and M.-C. Chen, "Extended phase matching of high harmonic generation by plasma-induced defocusing," Optica **4**, 976–981 (2017).
25. L. Hareli, L. Lobachinsky, G. Shoulga, Y. Eliezer, L. Michaeli, and A. Bahabad, "On-the-fly control of high-harmonic generation using a structured pump beam," Phys. Rev. Lett. **120**, 183902 (2018).
26. A. Zaïr, M. Holler, A. Guandalini, F. Schapper, J. Biegert, L. Gallmann, U. Keller, A. S. Wyatt, A. Monmayrant, I. A. Walmsley, E. Cormier, T. Auguste, J.-P. Caumes, and P. Salieres, "Quantum path interferences in high-order harmonic generation," Phys. Rev. Lett. **100**, 143902 (2008).
27. J. E. Kruse, P. Tzallas, E. Skantzakis, and D. Charalambidis, "Persistent quantum interfering electron trajectories," Phys. Rev. A **82**, 033438 (2010).
28. G. Kolliopoulos, B. Bergues, H. Schröder, P. A. Carpeggiani, L. Veisz, G. D. Tsakiris, D. Charalambidis, and P. Tzallas, "Revealing quantum path details in high-field physics," Phys. Rev. A **90**, 013822 (2014).
29. P. Balcou, P. Salieres, A. L'Huillier, and M. Lewenstein, "Generalized phase-matching conditions for high harmonics: the role of field-gradient forces," Phys. Rev. A **55**, 3204–3210 (1997).
30. C. M. Heyl, J. Güdde, U. Höfer, and A. L'Huillier, "Spectrally resolved maker fringes in high-order harmonic generation," Phys. Rev. Lett. **107**, 033903 (2011).
31. C. Corsi, A. Pirri, E. Sali, A. Tortora, and M. Bellini, "Direct interferometric measurement of the atomic dipole phase in high-order harmonic generation," Phys. Rev. Lett. **97**, 023901 (2006).
32. J. Lu, E. F. Cunningham, Y. S. You, D. A. Reis, and S. Ghimire, "Interferometry of dipole phase in high harmonics from solids," Nat. Photonics **13**, 96–100 (2018).
33. P.-C. Huang, C. Hernández-García, J.-T. Huang, P.-Y. Huang, C.-H. Lu, L. Rego, D. D. Hickstein, J. L. Ellis, A. Jaron-Becker, A. Becker, S. D. Yang, C. G. Durfee, L. Plaja, H. C. Kapteyn, M. M. Murnane, A. H. Kung, and M.-C. Chen, "Polarization control of isolated high-harmonic pulses," Nat. Photonics **12**, 349–354 (2018).
34. R. M. A. Azzam and B. J. Thompson, *Selected Papers on Ellipsometry*, Vol. 27 of SPIE Milestone Series (SPIE, 1991).
35. H. Tompkins and E. A. Irene, *Handbook of Ellipsometry* (William Andrew, Elsevier, 2005).
36. T. Koide, T. Shidara, M. Yuri, N. Kandaka, K. Yamaguchi, and H. Fukutani, "Elliptical-polarization analyses of synchrotron radiation in the 5–80-eV region with a reflection polarimeter," Nucl. Instrum. Methods Phys. Res., Sect. A **308**, 635–644 (1991).
37. A. Ferré, C. Handschin, M. Dumergue, F. Burgy, A. Comby, D. Descamps, B. Fabre, G. A. Garcia, R. Géneaux, L. Merceron, E. Mével, L. Nahon, S. Petit, B. Pons, D. Staedter, S. Weber, T. Ruchon, V. Blanchet, and Y. Mairesse, "A table-top ultrashort light source in the extreme ultraviolet for circular dichroism experiments," Nat. Photonics **9**, 93–98 (2015).
38. T. Hahn, J. Bierbach, C. Rödel, D. Hemmers, M. Yeung, B. Dromey, S. Fuchs, A. Galestian, S. Kuschel, M. Zepf, G. G. Paulus, and G. Pretzler, "Broadband XUV polarimetry of high harmonics from plasma surfaces using multiple Fresnel reflections," Appl. Phys. B **118**, 241–245 (2015).
39. K. Veyrinas, C. Elkharrat, S. Marggi Poullain, N. Saquet, D. Dowek, R. R. Lucchese, G. A. Garcia, and L. Nahon, "Complete determination of the state of elliptically polarized light by electron-ion vector correlations," Phys. Rev. A **88**, 063411 (2013).

40. L. Barreau, K. Veyrinas, V. Gruson, S. J. Weber, T. Auguste, J.-F. Hergott, F. Lepetit, B. Carré, J.-C. Houver, D. Dowek, and P. Salières, "Evidence of depolarization and ellipticity of high harmonics driven by ultrashort bichromatic circularly polarized fields," Nat. Commun. **9**, 4727 (2018).
41. C. Hernández-García, J. S. Román, L. Plaja, and A. Picón, "Quantum-path signatures in attosecond helical beams driven by optical vortices," New J. Phys. **17**, 093029 (2015).
42. L. Rego, J. S. Román, A. Picón, L. Plaja, and C. Hernández-García, "Nonperturbative twist in the generation of extreme-ultraviolet vortex beams," Phys. Rev. Lett. **117**, 163202EP (2016).
43. L. Rego, K. M. Dorney, N. J. Brooks, Q. L. Nguyen, C.-T. Liao, J. San Román, D. E. Couch, A. Liu, E. Pisanty, M. Lewenstein, L. Plaja, H. C. Kapteyn, M. M. Murnane, and C. Hernández-García, "Generation of extreme-ultraviolet beams with time-varying orbital angular momentum," Science **364**, eaaw9486 (2019).
44. D. D. Hickstein, F. J. Dollar, P. Grychtol, J. L. Ellis, R. Knut, C. Hernández-García, D. Zusin, C. Gentry, J. M. Shaw, T. Fan, K. M. Dorney, A. Becker, A. Jaron-Becker, H. C. Kapteyn, M. M. Murnane, and C. G. Durfee, "Non-collinear generation of angularly isolated circularly polarized high harmonics," Nat. Photonics **9**, 743–750 (2015).
45. C. Hernández-García, C. G. Durfee, D. D. Hickstein, T. Popmintchev, A. Meier, M. M. Murnane, H. C. Kapteyn, I. J. Sola, A. Jaron-Becker, and A. Becker, "Schemes for generation of isolated attosecond pulses of pure circular polarization," Phys. Rev. A **93**, 043855 (2016).
46. M. B. Gaarde, J. L. Tate, and K. J. Schafer, "Macroscopic aspects of attosecond pulse generation," J. Phys. B **41**, 132001 (2016).
47. A. Fleischer, O. Kfir, T. Diskin, P. Sidorenko, and O. Cohen, "Spin angular momentum and tunable polarization in high-harmonic generation," Nat. Photonics **8**, 543–549 (2014).
48. J. L. Ellis, K. M. Dorney, D. D. Hickstein, N. J. Brooks, C. Gentry, C. Hernández-García, D. Zusin, J. M. Shaw, Q. L. Nguyen, C. A. Mancuso, G. S. M. Jansen, S. Witte, H. C. Kapteyn, and M. M. Murnane, "High harmonics with spatially varying ellipticity," Optica **5**, 479–485 (2018).
49. D. Azoury, O. Kneller, M. Krüger, B. D. Bruner, O. Cohen, Y. Mairesse, and N. Dudovich, "Interferometric attosecond lock-in measurement of extreme-ultraviolet circular dichroism," Nat. Photonics **13**, 198–204 (2019).
50. L. Rego, J. S. Román, L. Plaja, A. Picón, and C. Hernández-García, "Ultrashort extreme ultraviolet vortices," in *Vortex Dynamics and Optical Vortices*, H. Perez-de-Tejada, ed. (IntechOpen, 2017), Chapter 9.
51. T. Kanai, E. J. Takahashi, Y. Nabekawa, and K. Midorikawa, "Destructive interference during high harmonic generation in mixed gases," Phys. Rev. Lett. **98**, 153904 (2007).
52. D. Azoury, O. Kneller, S. Rozen, B. D. Bruner, A. Clergerie, Y. Mairesse, B. Fabre, B. Pons, N. Dudovich, and M. Krüger, "Electronic wavefunctions probed by all-optical attosecond interferometry," Nat. Photonics **13**, 54–61 (2018).
53. M. V. Ammosov, N. B. Delone, and V. P. Karinov, "Tunnel ionization of complex atoms and of atomic ions in an alternating electromagnetic field," Sov. Phys. JETP **64**, 1191 (1987).
54. E. Bordo, O. Neufeld, O. Kfir, A. Fleischer, and O. Cohen, "Spectroscopy of atomic orbital sizes using bi-elliptical high-order harmonic generation," Phys. Rev. A **100**, 043419EP (2019).
55. N. Klemke, N. Tancogne-Dejean, G. M. Rossi, Y. Yang, F. Scheiba, R. E. Mainz, G. Sciacca, A. Rubio, F. X. Kärtner, and O. D. Mücke, "Polarization-state-resolved high-harmonic spectroscopy of solids," Nat. Commun. **10**, 1–7 (2019).
56. D. Ayuso, O. Neufeld, A. F. Ordonez, P. Decleva, G. Lerner, O. Cohen, M. Ivanov, and O. Smirnova, "Synthetic chiral light for efficient control of chiral light–matter interaction," Nat. Photonics **13**, 866–871 (2019).